European Radiology
https://doi.org/10.1007/s00330-022-09088-5

MAGNETIC RESONANCE

Optimisation of *b*-values for the accurate estimation of the apparent diffusion coefficient (ADC) in whole-body diffusion-weighted MRI in patients with metastatic melanoma

Annemarie K. Knill[1,2] · Matthew D. Blackledge[1] · Andra Curcean[1,2] · James Larkin[2] · Samra Turajlic[2,3] · Angela Riddell[2] · Dow Mu Koh[1,2] · Christina Messiou[1,2] · Jessica M. Winfield[1,2]

Received: 29 March 2022 / Revised: 12 July 2022 / Accepted: 4 August 2022

Abstract

Objective To establish optimised diffusion weightings ('*b*-values') for acquisition of whole-body diffusion-weighted MRI (WB-DWI) for estimation of the apparent diffusion coefficient (ADC) in patients with metastatic melanoma (MM). Existing recommendations for WB-DWI have not been optimised for the tumour properties in MM; therefore, evaluation of acquisition parameters is essential before embarking on larger studies.

Methods Retrospective clinical data and phantom experiments were used. Clinical data comprised 125 lesions from 14 examinations in 11 patients with multifocal MM, imaged before and/or after treatment with immunotherapy at a single institution. ADC estimates from these data were applied to a model to estimate the optimum *b*-value. A large non-diffusing phantom was used to assess eddy current–induced geometric distortion.

Results Considering all tumour sites from pre- and post-treatment examinations together, metastases exhibited a large range of mean ADC values, $[0.67–1.49] \times 10^{-3}$ mm^2/s, and the optimum high *b*-value (b_{high}) for ADC estimation was 1100 (10th–90th percentile: 740–1790) s/mm^2. At higher *b*-values, geometric distortion increased, and longer echo times were required, leading to reduced signal.

Conclusions Theoretical optimisation gave an optimum b_{high} of 1100 (10th–90th percentile: 740–1790) s/mm^2 for ADC estimation in MM, with the large range of optimum *b*-values reflecting the wide range of ADC values in these tumours. Geometric distortion and minimum echo time increase at higher *b*-values and are not included in the theoretical optimisation; b_{high} in the range 750–1100 s/mm^2 should be adopted to maintain acceptable image quality but performance should be evaluated for a specific scanner.

Key Points

- *Theoretical optimisation gave an optimum high b-value of 1100 (10th–90th percentile: 740–1790) s/mm^2 for ADC estimation in metastatic melanoma.*
- *Considering geometric distortion and minimum echo time (TE), a b-value in the range 750–1100 s/mm^2 is recommended.*
- *Sites should evaluate the performance of specific scanners to assess the effect of geometric distortion and minimum TE.*

Keywords Diffusion magnetic resonance imaging · Apparent diffusion coefficient · Whole-body imaging · Melanoma · Metastasis

CM and JMW contributed equally as joint lead authors.

✉ Christina Messiou
christina.messiou@rmh.nhs.uk

[1] The Institute of Cancer Research, London, UK

[2] The Royal Marsden NHS Foundation Trust, London, UK

[3] The Francis Crick Institute, London, UK

Abbreviations

ADC	Apparent diffusion coefficient
DI	Distortion index
DWI	Diffusion-weighted imaging
MM	Metastatic melanoma
PDMS	Polydimethylsiloxane
ROI	Region of interest
Rx	Treatment
SE-EPI	Spin Echo - Echo Planar imaging

Published online: 28 September 2022

SNR	Signal-to-noise ratio
SPAIR	Spectral Attenuated Inversion Recovery
STIR	Short T_1 inversion recovery
TE	Echo time
TR	Repetition time
WB-DWI	Whole-body diffusion-weighted MRI

Introduction

Whole-body MRI with diffusion-weighted imaging (WB-DWI) has emerged as a powerful tool for monitoring patients with advanced cancers because it offers combined morphological and quantitative information within a single radiological exam [1, 2]. It has a favourable safety profile, due to the lack of ionising radiation used in other techniques such as CT and PET-CT, and a good diagnostic performance [3, 4]. WB-MRI offers an increased overall specificity and sensitivity in the liver, subcutaneous and intramuscular lesions over CT [5]. Acquiring images with at least two diffusion weightings ('*b*-values') enables quantification of the apparent diffusion coefficient (ADC), a surrogate biomarker of tumour cellularity. Inclusion of WB-DWI in imaging guidelines [6–8] for staging and response evaluation in myeloma and metastatic prostate cancer has triggered standardised protocols optimised for those applications [1, 2, 9]. The lack of ionising radiation has also seen WB-DWI evaluated as a screening tool for patients with high risk of developing cancer [10, 11].

WB-DWI has not yet been extensively investigated in metastatic melanoma (MM), and current evidence is therefore limited. An evaluation of the imaging characteristics in these patients is required to determine a suitable protocol before WB-DWI can be used for larger studies in patients with MM, because there is no guarantee that existing protocols will be suitable for imaging MM. However, WB-DWI has great potential for detecting small volume disease in these patients and has already been included in some national guidelines for imaging paediatric patients [12].

Immunotherapy in the form of the immune checkpoint inhibitors ipilimumab, nivolumab and pembrolizumab has improved survival for patients with MM but introduces new challenges when imaging response. Atypical response patterns include disease shrinkage after initial increase in tumour burden, and shrinkage after appearance of new lesions; the reported incidence of this 'pseudoprogression' is up to 10% [13]. Potential for highly morbid toxicities [14, 15] and the cost of treatment accentuate the challenges of maintaining patients on a therapy where therapeutic benefit is uncertain for individual patients.

WB-DWI offers potential as a sensitive staging tool and whole-body estimates of tumour ADC may also reflect response to treatment independent of changes in lesion size [16]. However, to date there is insufficient data to allow optimisation of *b*-values for ADC estimation and response assessment of MM.

The aim of this study was to establish optimised *b*-values for the acquisition of WB-DWI for ADC estimation in patients with MM, using retrospective patient data and phantom experiments. It was also necessary to assess the practical implementation and the effects on image quality, including geometric distortion and signal-to-noise ratio (SNR), when acquiring images with optimum *b*-values on clinical MRI scanners.

Materials and methods

Clinical studies

A retrospective single-institution study was performed, with the requirement for written informed consent waived by the institution. All patients with an established diagnosis of MM who underwent an MRI examination of the whole body or abdomen and pelvis including diffusion-weighted imaging (DWI) between May 2017 and February 2019 were included. Patients with previously treated and untreated disease were included. None of the scans were excluded. Images were acquired on either a 1.5-T or 3-T scanner (MAGNETOM Aera, Avanto and Skyra, Siemens Healthcare) (Table 1).

For each patient, regions of interest (ROIs) were drawn around all tumours larger than 1 cm in size on $b = 50$ s/mm^2 images on all tumour containing image slices and checked by a radiologist with > 1 year of experience in WB-DWI (Fig. 1). ROIs were drawn using Horos (horosproject.org), and morphological sequences were used as reference. The minimum tumour diameter of 1 cm was chosen for ROIs to avoid partial volume effects. ADCs were estimated using a mono-exponential decay model fitted to the logarithm of the DWI signal at all *b*-values using a least squares fit (SciPy [17]). The mean ADC of all fitted voxels in the ROIs was estimated for each tumour.

Image and data analysis

Using error propagation and the definition of the ADC, Bito et al proposed a model for the standard deviation in the ADC when images are acquired with at least two *b*-values,

$$\mathrm{SD}(D) = D_0\sigma\frac{\sqrt{\sum_{n=1}^{N}\left(Nx_n-\sum_{i=1}^{N}x_i\right)^2\exp(2x_n)}}{N\sum_{n=1}^{N}{x_n}^2-\left(\sum_{n=1}^{N}x_n\right)^2}, \quad (1)$$

where b_{low} is the lowest *b*-value used, $x_n = D_0 b$ are the scaled gradient factors, σ is the standard deviation of the signal in the

Table 1 MRI acquisition parameters

Scanning parameters	WB-DWI	Abdo/pelvis		
		A	B	C
B_0 field strength (T)	1.5	3	1.5	1.5
Scanner model	Aera	Skyra	Aera	Avanto
Sequence	SE-EPI	SE-EPI	SE-EPI	SE-EPI
Orientation	Axial	Axial	Axial	Axial
b-values (s/mm^2)	50, 600, 900	50, 600, 900	50, 600, 900	50, 600, 900, 1050
Diffusion gradient scheme	Monopolar	Bipolar	Monopolar	Bipolar
Diffusion encoding scheme [a]	Four-scan trace	Three-scan trace	Four-scan trace	Three-scan trace
Echo time (ms)	64	70	61	71
Repetition time (ms)	6150	10,900	10,200	8000
Slices per station/stations	40/6	50/2	50/2	50/3
Slice thickness (mm)	5	5.5	5 or 6	5
Slice gap (mm)	0	0	0	0
Field of view (mm)	354 × 439 or 346 × 430	313 × 380	446 × 439	420 × 341
Reconstructed matrix (mm × mm)	268 × 216	320 × 264	272 × 268	256 × 208
Acquisition matrix (mm × mm)	134 × 108	160 × 132	136 × 134	128 × 104
Fat suppression	STIR	SPAIR	SPAIR	SPAIR
Breathing instructions	Free breathing	Free breathing	Free breathing	Free breathing
Number of signal averages per *b*-value	2, 2, 4	1, 3, 3	2, 2, 4	3, 3, 3, 3
Patients	**5**	**3**	**2**	**1**

[a] Three-scan trace employs three mutually orthogonal diffusion gradient directions, which are not aligned with the cardinal axes of the scanner; four-scan trace is an implementation of the tetrahedral diffusion encoding scheme [30]

All scanners made by Siemens Healthcare. *SE-EPI*, Spin Echo - Echo Planar imaging; *STIR*, short T_1 inversion recovery; *SPAIR*, spectral adiabatic inversion recovery

image acquired with b_{low}, D_0 is the true ADC, and N is the number of image acquisitions [18]. This model assumes that signal attenuation follows mono-exponential decay with *b*-value and that noise in the signal is normally distributed with variance σ^2. It provides a general description of the variation in SD(D) given any combination of *b*-values; however, optimisation yields a solution requiring only two: b_{low} and b_{high}. From Eq. 1, the optimum ratio, R, of the number of image acquisitions at the low to high *b*-value is 1:3 [18]. The optimum value of b_{low} is 0 s/mm^2; however, many authors choose 50 s/mm^2 to reduce the influence of perfusion [18, 19].

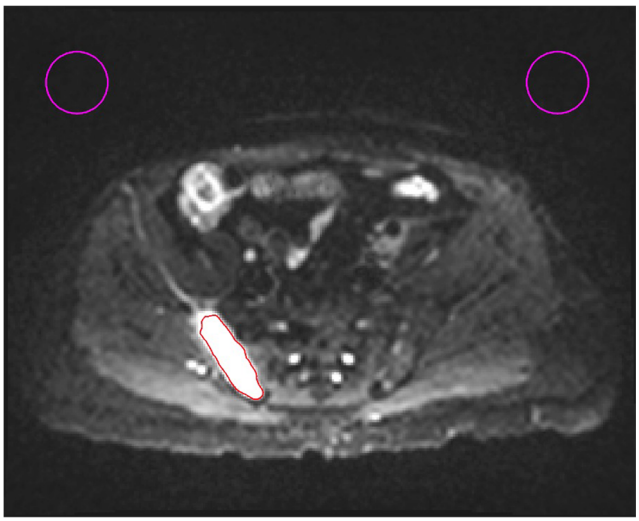

Fig. 1 An example of the ROIs drawn (pink) on DWI $b = 50$ s/mm^2 image to estimate the noise. The lesion is delineated in red. The number of pixels in the ROIs was kept constant across the different matrix sizes used

In each of the $b = 50$ s/mm^2 images in which the tumours were delineated, two identical circular ROIs were drawn in a region of background, away from signal, ghosts and unsuppressed fat (Fig. 1). The value of σ was estimated by taking the standard deviation of all pixels in the background ROIs. The mean tumour ADCs of the voxels in the delineated lesions were calculated as an estimate of the population ADC, D_0, in each sub-group of the lesions, split by tissue type and scanning time point, and overall.

The optimum high *b*-value (b_{opt}) was estimated computationally as the value of b_{high} which minimised SD(D) calculated for b_{high} in the range 400–2500 s/mm^2 with b_{low} = 50 s/mm$_2$, N = 24 and R = 1:3. The value of b_{opt} was estimated using σ and D_0 calculated from each sub-group of the lesions and overall. The validity of the model was confirmed experimentally by comparing the measured

standard deviation of the ADC of a uniform phantom to the prediction made using the model (as detailed in the Supplementary Materials).

Phantom studies

Variation in echo time with *b*-value

The minimum achievable echo time (TE) and corresponding repetition time (TR) were noted for high *b*-values in the range 700–1800 s/mm^2 (lowest *b*-value = 50 s/mm^2, FOV = 500 × 500 mm^2, and matrix size = 124 × 138, MAGNETOM Aera Scanner, Siemens Healthcare).

Evaluation of *b*-value dependence on geometric distortion

Geometric distortion was assessed using a large phantom containing polydimethylsiloxane (PDMS) [20, 21]. Axial DWI was acquired with TR = 11,200 ms, TE = 80 ms and *b*-values 0, 900, 1050, 1150 and 1250 s/mm^2 using multi-directional diffusion weightings and bipolar gradients with 12 diffusion encoding directions. ROIs were drawn on subtraction images (the signal intensity of the $b = 0$ s/mm^2 minus the high *b*-value image) around the phantom and a region of noise (Fig. 2). A semi-quantitative distortion index (DI) was calculated by counting the number of pixels in the phantom ROI which had a value 3 times greater than the standard deviation of the pixels in the noise ROI and dividing by a factor of 1000.

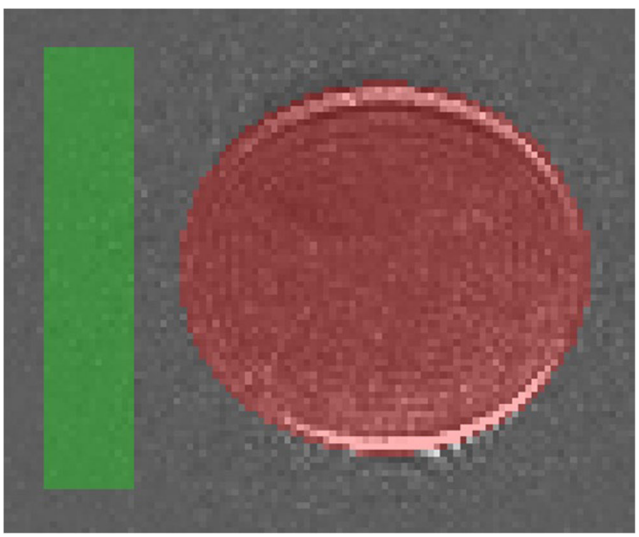

Fig. 2 An example of the ROIs drawn on the DWI subtraction images to calculate the semi-quantitative distortion index using a PDMS phantom. ROIs are drawn in the signal region (376 cm^2, red) and in a region of noise (130 cm^2, green) on a single central slice. Axial DWI was acquired with TR = 11,200 ms, TE = 80 ms and *b*-values 0, 900, 1050, 1150 and 1250 s/mm^2 using multi-directional diffusion weightings, bipolar gradients with 12 diffusion encoding directions

Results

Clinical studies

Eleven patients with MM, 6 males and 5 females with a mean age of 58 years (range 22–73 years), underwent MRI investigations. These included 5 previously treated patients (3 males, 2 females) and 6 untreated patients (3 males, 3 females). None of the patients had previous or coexisting malignancies. Three patients had baseline and post-immunotherapy scans; 4 patients had baseline scans only; 4 patients had a single post-treatment scan. Of the patients with post-treatment scans, 3 were treated with pembrolizumab (1 reported as response, 1 stable disease, 1 progression), 1 with ipilimumab (progression) and 3 with a combination of ipilimumab and nivolumab (1 reported as response, 1 stable disease, 1 progression, later confirmed as pseudoprogression). The mean time between the most recent cycle of immunotherapy and the post-treatment scan was 92 days (range: 7–250 days). Eight patients were scanned at 1.5 T and three patients scanned at 3 T. Of these patients, five were scanned with whole-body coverage and six covering the abdomen and pelvis. The volume and distribution of disease are outlined in Table 2. A total of 125 lesions were analysed in this study, with the most common locations of metastasis being the bone, liver and lymph nodes.

The mean ADC estimates from sites of disease at different anatomical locations are summarised in Table 3. The lowest mean ADC was calculated for the group 'other' (two presacral nodules) 0.67 × 10^{-3} mm^2/s, and the highest mean ADC was in intramuscular deposits, 1.49 × 10^{-3} mm^2/s.

The value of b_{opt} is estimated to be 1100 (10th and 90th percentile: 740–1790) s/mm^2 considering lesions at all timepoints and locations, as shown in Fig. 3.

Phantom studies

Variation in TE with *b*-value

For the sequence described, at $b = 700$ s/mm^2 the minimum TE was 68 ms with TR = 6270 ms, and at $b = 1800$ s/mm^2 the minimum TE was 81 ms with TR = 6372 ms. The minimum TE increases with the *b*-value in the evaluated range (700–1800 s/mm^2).

Evaluation of the *b*-value dependence of distortion

The subtraction images calculated using the PDMS phantom are shown in Fig. 4. Figure 5 shows the results of the analysis using two ROIs specified in Fig. 2. While there is a large amount of variation in the semi-quantitative DI at different encoding directions, the mean of the DI across all diffusion encoding directions for a given *b*-value is noticeably higher at

Table 2 Distribution and volume of the analysed lesions

	No. of patients			No. of Tumours			Median lesion volume (cm3)		
Location	Pre Rx	Post Rx	Overall	Pre Rx	Post Rx	Overall	Pre Rx	Post Rx	Overall
Bone	3	4	5	29	19	48	22.9 (7.81–248)	16.0 ((8.07–471)	19.7 (7.81–471)
Liver	4	3	4	21	26	47	26.6 (11.1–53,900)	156 (16.1–71,200)	57.3 (16.1–71,200)
Lymph nodes	4	3	4	5	5	10	121 (8.96–929)	183 (17.9–2130)	126 (8.96–2130)
Bowel/Peritoneum	2	4	6	2	5	7	609 (18.6–1200)	59.7 (13.6–205)	60 (13.6–1200)
Lung	2	1	2	3	1	4	109 (25.2–4060)	5670	2080 (25.2–5670)
Kidney	0	2	2		2	2		16.0 (7.93–24.0)	16.0 (7.93–24.0)
Subcutaneous	1	1	1	1	1	2	31.4	22.8	27.1 (22.8–31.4)
Muscle	1	2	2	0	2	2		1250 (310–2200)	1250 (310–2200)
Other	2	0	2	2	0	2	24.5 (17.6–31.5)		24.5 (17.6–31.5)
Adrenal		1	1	0	1	1		41	41
Overall	**7**	**7**	**11**	**63**	**62**	**125**	**28.3 (7.81–53,900)**	**64.1 (7.93–71,200)**	**40.6 (7.81–71,200)**

Values in brackets show the range in volume. *Rx*, treatment

b-values = 1050, 1150, and 1250 s/mm^2 than at *b* = 900 s/mm^2.

Discussion

Protocol recommendations for WB-DWI in myeloma and metastatic prostate cancer recommend high *b*-values of 800–1000 s/mm^2 and 800–900 s/mm^2 respectively [1, 2]; however, a recommendation of the choice of *b*-values for use in MM has not yet been established. To achieve this, an estimation of the range of ADC values in these patients was necessary.

This retrospective study of patients with metastatic melanoma demonstrated that a large range of mean ADCs exists across disease sites and pre- and post-treatment: [0.67–1.49] × 10^{-3} mm^2/s and the overall mean ADC values calculated were comparable to the reported ADC of other tumour types, such as myeloma [22–24] and metastatic prostate cancer [25].

From this analysis, the theoretical optimum *b*-value for the estimation of ADC values in MM was 1100 (10th and 90th percentile: 740–1790) s/mm^2. The large range of mean ADCs in this disease type is reflected in the difference between the values of the 10th and 90th percentile of b_{opt}. Lesions with high ADC and short T_2 values will have very low signal at high *b*-values above 1100 s/mm^2, leading to noise bias in ADC estimation. Hence, a *b*-value in the range 750–1100 s/mm^2 is an appropriate compromise as it reduces the noise bias in these low signal regions, despite not being the optimum *b*-value for some lesions.

Table 3 Mean and 10th and 90th percentile of the ADCs

	Mean ADC (10^{-3} mm^2/s)		
Location	Pre Rx	Post Rx	Overall
Bone	0.91 (0.50–1.48)	1.33 (0.66–1.86)	1.11 (0.56–1.74)
Liver	1.13 (0.68–1.82)	1.20 (0.77–1.80)	1.18 (0.74–1.81)
Lymph nodes	1.42 (0.81–2.26)	1.29 (0.82–1.84)	1.32 (0.82–1.99)
Bowel/Peritoneum	0.91 (0.67–1.23)	0.85 (0.43–1.24)	0.90 (0.65–1.23)
Lung	1.11 (0.52–1.87)	1.08 (0.59–1.84)	1.10 (0.56–1.85)
Kidney		1.38 (0.99–1.79)	1.38 (0.99–1.79)
Subcutaneous	1.05 (0.65–1.66)	0.96 (0.73–1.31)	1.01 (0.69–1.45)
Muscle		1.49 (1.20–1.77)	1.49 (1.20–1.77)
Other	0.67 (0.48–0.86)		0.67 (0.48–0.86)
Adrenal		1.00 (0.50–1.54)	1.00 (0.50–1.54)
Overall	**1.12 (0.65–1.81)**	**1.20 (0.75–1.80)**	**1.18 (0.72–1.81)**

10th and 90th percentile in brackets. The group classified as 'other' includes two presacral nodules. *Rx*, treatment

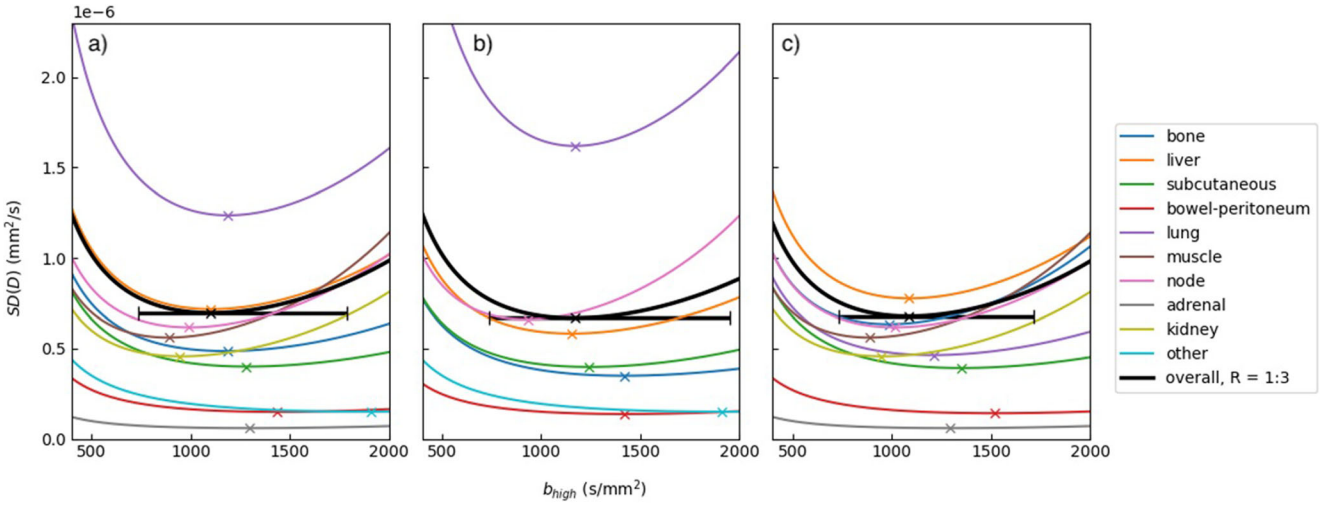

Fig. 3 From left to right, the standard deviation in the ADC plotted against b_{high} for all timepoints, pre-treatment lesions only and post-treatment lesions only, using a ratio, *R*, equal to the optimum value of 1:3 and b_{low} = 50 s/mm^2. The retrospective data is used to estimate the true ADC and D_0 and the number of image acquisitions, *N*, is 24. The minima of the curves (×) correspond to the predicted optimum *b*-value, b_{opt}, for each tumour type. The error bars on the minima of the curves represent the values of b_{opt} calculated using the 10th and 90th percentile of the retrospective ADC estimates. (On clinical MRI scanners, *b*-values are often specified in increments of 50 s/mm^2)

The *b*-value and the echo time (TE) of a DWI sequence are interrelated, so when the *b*-value is increased the TE also increases [26]. This influences the T_2 weighting of the images. However, the T_2 dependence of SD(*D*) is not examined in Eq. 1, and in order to apply any model which accounts for the dependence on T_2 (for example, Saritas et al [27]), the characteristic values of the T_2 relaxation time for melanoma tumours would be needed. Such information has not yet been published. The approximate signal loss can be estimated from the minimum values of TE, an estimate of T_2 for melanoma (41 ms, from a pre-clinical model [28]), and by considering only T_2 decay. This suggests that there would be ~27% lower signal in images acquired at TE = 81 ms (the minimum TE at *b* = 1800 s/mm^2, for the sequence investigated in this study) compared with images acquired at TE = 68 ms (the minimum TE at *b* = 700 s/mm^2).

It is also important to consider the increase in eddy current–induced distortion with *b*-value. Increased distortion at high *b*-values will impact the accuracy of the pixelwise ADC calculation because pixels are no longer aligned on the images acquired at different *b*-values [20]. The results from the PDMS phantom demonstrated mean distortion across all diffusion encoding directions was noticeably higher when acquiring images with *b*-values 1050, 1150 and 1250 s/mm^2 compared to acquisition with *b* = 900 s/mm^2.

Reduction in signal and increase in distortion at higher *b*-values can result in impaired image quality and degraded

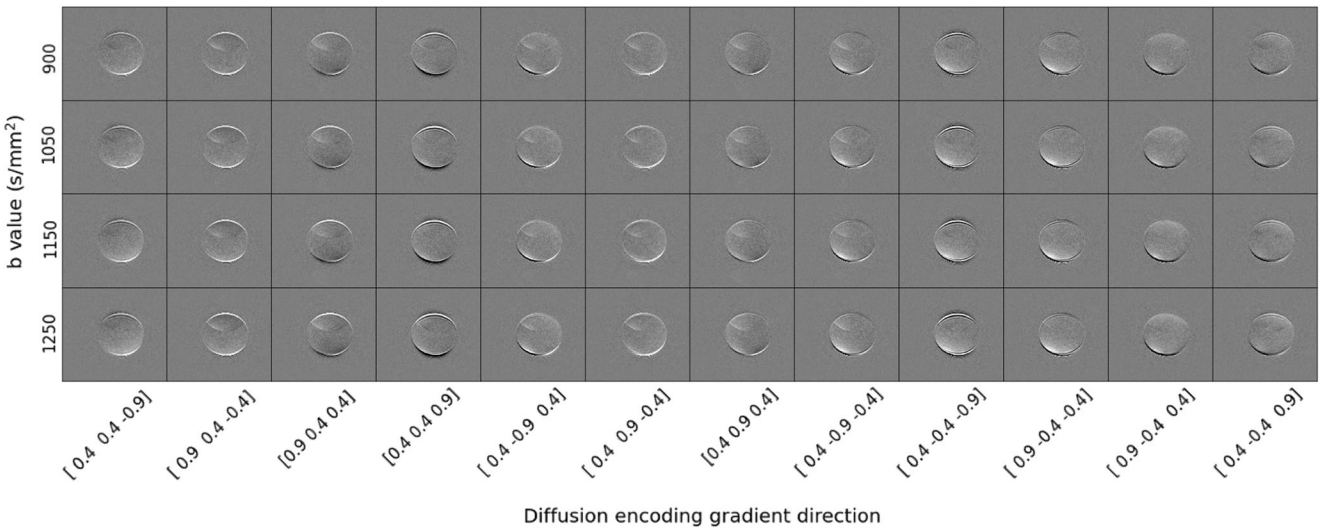

Fig. 4 Subtraction images, calculated by subtracting the signal intensity in the image with the given *b*-value and diffusion encoding direction from the image acquired at *b* = 0 s/mm^2. All images have the same window width and window level

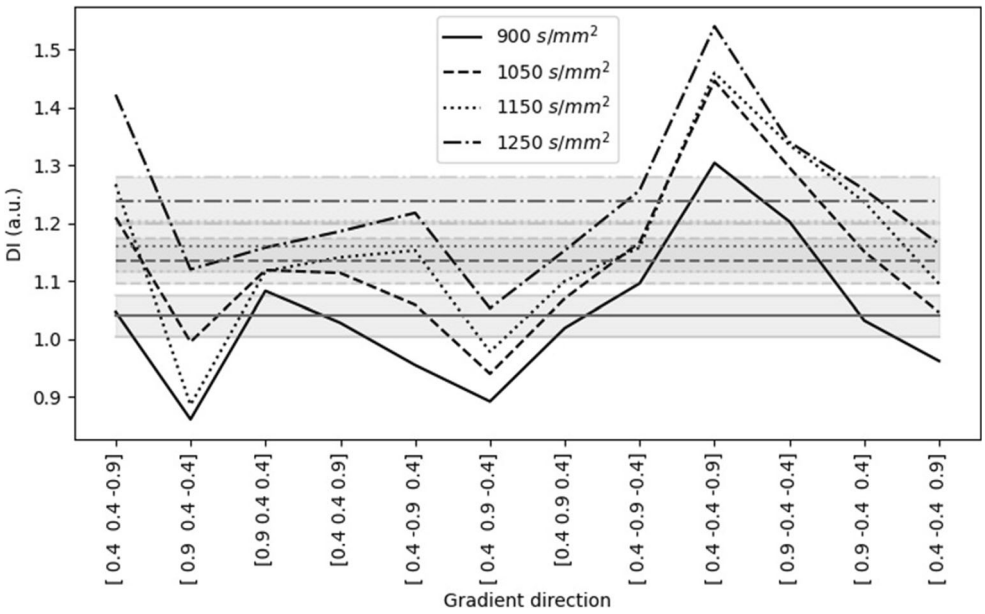

Fig. 5 The semi-quantitative distortion index calculated from DWI of a PDMS phantom when images are acquired with different gradient encoding directions, b_{low} = 0 s/mm^2 and b_{high} as shown in the figure legend. The horizontal grey lines represent the mean values across all diffusion encoding directions at the given *b*-value and the shaded regions show the corresponding standard error on these means

ADC estimates. Distortion and achievable TE effects are scanner dependent; therefore, centres may choose to assess the individual performance of their scanners before deciding on the high *b*-value for their protocol.

Most clinically adopted DWI protocols will also include a third *b*-value midway between the minimum and maximum values, usually around 600 s/mm^2 [1, 2]. This can be useful for the observation of soft tissues and can also be included in the calculation of the ADC.

The key limitation of this study was the heterogeneity of the retrospective data due to variations in the scanner, field strength and parameters. Whilst these differences may affect properties such as SNR, diffusion times and fat signal, the differences between parameters are relatively small (comparable to the ranges specified in the QIBA liver profile [29]) and reflect the variation in imaging protocols used for different body parts and scanners. Additionally, the ADC is not dependent on the field strength and the TR in all protocols was sufficiently long to allow for T_1 recovery. Therefore, variation in these parameters is not expected to have a marked impact on the presented results.

Furthermore, the differences in parameters across the protocols reflect the nature of real-world data. This is in some ways an advantage; the recommendations we draw from this cohort have been derived from a mixture of data; therefore, the values of the mean ADC and noise in the images are not biased towards one protocol. The optimisation of the technical aspects of the imaging protocol presented here provides an ideal starting point for the collection of larger data sets in this patient population.

Moreover, with the advent of immunotherapy treatment, the proportion of MM patients who receive systemic treatment is increasing. Therefore, the characterisation of melanoma lesions both pre- and post-treatment is important to ensure the proposed *b*-values are appropriate for this group of patients at all stages of treatment.

In conclusion, the analysis of the retrospective data has demonstrated that there is a large range of mean ADC values which are characteristic of MM. Using only a theoretical model, a high *b*-value of 1100 (10th and 90th percentile: 740–1790) s/mm^2 with b_{low} = 50 s/mm^2 was determined to be optimal for ADC calculation; however, due to the additional considerations of increased distortion and minimum TE at high *b*-values, we recommend b_{high} is chosen in the range 750–1100 s/mm^2 and individual sites should assess the performance of their scanners before choosing a value for their protocol.

Supplementary Information The online version contains supplementary material available at https://doi.org/10.1007/s00330-022-09088-5.

Funding We acknowledge CRUK and EPSRC support to the Cancer Imaging Centre at ICR and RMH in association with MRC and Department of Health (C1060/A10334, C1060/A16464) and NHS funding to the NIHR Biomedical Research Centre and the NIHR Royal Marsden Clinical Research Facility in Imaging. This report is independent research funded by the National Institute for Health Research. The views expressed in this publication are those of the authors and not necessarily those of the NHS, the National Institute for Health Research or the Department of Health.

Declarations

Guarantor The scientific guarantor of this publication is Christina Messiou.

Conflict of interest M. D. Blackledge is a director and shareholder of Diafora Medical, a medical technology company in a broadly related field. M. D. Blackledge has, or has had within the past 5 years, consultancy contracts with medical companies developing solutions in a broadly related field.

He is also a member of the European Radiology Editorial Board. He has not taken part in the review or selection process of this article.

The other authors of this manuscript declare no relationships with any companies whose products or services may be related to the subject matter of the article.

Statistics and biometry No complex statistical methods were necessary for this paper.

Informed consent Written informed consent was waived by the Institutional Review Board.

Ethical approval Institutional Review Board approval was obtained.

Methodology
- retrospective
- observational
- performed at one institution

References

1. Padhani AR, Lecouvet FE, Tunariu N et al (2017) METastasis Reporting and Data System for Prostate Cancer: practical guidelines for acquisition, interpretation, and reporting of whole-body magnetic resonance imaging-based evaluations of multiorgan involvement in advanced prostate cancer. Eur Urol 71:81–92
2. Messiou C, Hillengass J, Delorme S et al (2019) Guidelines for acquisition, interpretation, and reporting of whole-body MRI in myeloma: Myeloma Response Assessment and Diagnosis System (MY-RADS). Radiology 291:5–13
3. Taylor SA, Mallett S, Beare S et al (2019) Diagnostic accuracy of whole-body MRI versus standard imaging pathways for metastatic disease in newly diagnosed colorectal cancer: the prospective Streamline C trial. Lancet Gastroenterol Hepatol 4:529–537
4. Taylor SA, Mallett S, Ball S et al (2019) Diagnostic accuracy of whole-body MRI versus standard imaging pathways for metastatic disease in newly diagnosed non-small-cell lung cancer: the prospective Streamline L trial. Lancet Respir Med 7:523–532
5. Hausmann D, Jochum S, Utikal J et al (2011) Comparison of the diagnostic accuracy of whole-body MRI and whole-body CT in stage III/IV malignant melanoma. JDDG - J Ger Soc Dermatology 9:212–221
6. Rajkumar SV, Dimopoulos MA, Palumbo A et al (2014) International Myeloma Working Group updated criteria for the diagnosis of multiple myeloma. Lancet Oncol 15:e538–e548
7. NICE Recommendations | Myeloma: diagnosis and management | Guidance. https://www.nice.org.uk/guidance/ng35. Accessed 1 Apr 2021
8. Trabulsi EJ, Rumble RB, Jadvar H et al (2020) Optimum imaging strategies for advanced prostate cancer: ASCO guideline. J Clin Oncol 38:1963–1996
9. Barnes A, Alonzi R, Blackledge M et al (2018) UK quantitative WB-DWI technical workgroup: consensus meeting recommendations on optimisation, quality control, processing and analysis of quantitative whole-body diffusion-weighted imaging for cancer. Br J Radiol 91:20170577
10. Consul N, Amini B, Ibarra-Rovira JJ et al (2021) Li-Fraumeni syndrome and whole-body MRI screening: screening guidelines, imaging features, and impact on patient management. AJR Am J Roentgenol 216:252–263
11. Petralia G, Padhani AR, Pricolo P et al (2019) Whole-body magnetic resonance imaging (WB-MRI) in oncology: recommendations and key uses. Radiol Med 124:218–233
12. NICE Recommendations| Melanoma: assessment and management. https://www.nice.org.uk/guidance/ng14/chapter/1-Recommendations#staging-investigations-2. Accessed 2 Dec 2021
13. Wolchok JD, Hoos A, O'Day S et al (2009) Guidelines for the evaluation of immune therapy activity in solid tumors: immune-related response criteria. Clin Cancer Res 15:7412–7420
14. Larkin J, Chiarion-Sileni V, Gonzalez R et al (2019) Five-year survival with combined nivolumab and ipilimumab in advanced melanoma. N Engl J Med 381:1535–1546
15. O'Reilly A, Hughes P, Mann J et al (2020) An immunotherapy survivor population: health-related quality of life and toxicity in patients with metastatic melanoma treated with immune checkpoint inhibitors. Support Care Cancer 28:561–570
16. Lupo JM (2020) Diffusion MRI as an early marker of response to immune checkpoint inhibitors. Neuro Oncol 22:1557–1558
17. Virtanen P, Gommers R, Oliphant TE et al (2020) SciPy 1.0: fundamental algorithms for scientific computing in Python. Nat Methods 17:261–272
18. Bito Y, Hirata S, Yamamoto E (1995) Optimum gradient factors for apparent diffusion coefficient measurements. Proc Intl Soc Mag Reson Med 913
19. Koh DM, Blackledge M, Padhani AR et al (2012) Whole-body diffusion-weighted MRI: tips, tricks, and pitfalls. AJR Am J Roentgenol 199:252–262
20. Haselgrove JC, Moore JR (1996) Correction for distortion of echo-planar images used to calculate the apparent diffusion coefficient. Magn Reson Med 36:960–964
21. Winfield JM, Collins DJ, Priest AN et al (2016) A framework for optimization of diffusion-weighted MRI protocols for large field-of-view abdominal-pelvic imaging in multicenter studies. Med Phys 43:95–110
22. Messiou C, Collins DJ, Morgan VA, Desouza NM (2011) Optimising diffusion weighted MRI for imaging metastatic and myeloma bone disease and assessing reproducibility. Eur Radiol 21:1713–1718
23. Horger M, Weisel K, Horger W et al (2011) Whole-body diffusion-weighted MRI with apparent diffusion coefficient mapping for early response monitoring in multiple myeloma: Preliminary results. AJR Am J Roentgenol 196:W790–W795
24. Lacognata C, Crimì F, Guolo A et al (2017) Diffusion-weighted whole-body MRI for evaluation of early response in multiple myeloma. Clin Radiol 72:850–857

25. Messiou C, Collins DJ, Giles S et al (2011) Assessing response in bone metastases in prostate cancer with diffusion weighted MRI. Eur Radiol 21:2169–2177
26. Güllmar D, Haueisen J, Reichenbach JR (2005) Analysis of b-value calculations in diffusion weighted and diffusion tensor imaging. Concepts Magn Reson Part A Bridg Educ Res 25:53–66
27. Saritas EU, Lee JH, Nishimura DG (2011) SNR dependence of optimal parameters for apparent diffusion coefficient measurements. IEEE Trans Med Imaging 30:424–437
28. Gauvain KM, Garbow JR, Song SK et al (2005) MRI detection of early bone metastases in B16 mouse melanoma models. Clin Exp Metastasis 22:403–411
29. Shukla-Dave A, Obuchowski NA, Chenevert TL et al (2019) Quantitative imaging biomarkers alliance (QIBA) recommendations for improved precision of DWI and DCE-MRI derived biomarkers in multicenter oncology trials. J Magn Reson Imaging 49: e101–e121
30. Conturo TE, McKinstry RC, Akbudak E, Robinson BH (1996) Encoding of anisotropic diffusion with tetrahedral gradients: a general mathematical diffusion formalism and experimental results. Magn Reson Med 35:399–412